


Density functional calculations for structures and energetics of atomic steps and their implication for surface morphology on Si-face SiC polar surfaces

Kaori Seino ^{1,2} and Atsushi Oshiyama ¹¹*Institute of Materials and Systems for Sustainability, Nagoya University, Furo-cho, Chikusa-ku, Nagoya 464-8601, Japan*²*X-Ability Co., Ltd., Hongo, Bunkyo-ku, Tokyo 113-0033, Japan*

(Received 15 March 2020; revised manuscript received 17 April 2020; accepted 1 May 2020; published 19 May 2020)

We perform large-scale density-functional calculations using the real-space finite-difference scheme endorsed by the Gordon Bell prize in 2011 that reveal detailed atomic and electronic structures of atomic steps on silicon carbide (SiC) polar surfaces for the first time. The accurate structural optimization elucidates characteristic atomic reconstruction among the upper and lower edge atoms, which is peculiar to compound semiconductors having both covalent and ionic nature. The calculated formation energies of all the possible atomic steps lead us to unequivocally identify the abundant atomic steps on the Si-face SiC polar surfaces. The energetics thus obtained for the atomic steps provides a natural and persuasive microscopic reason for the difference in the step morphology observed experimentally, i.e., the meandering and straight step edges depending on the inclined direction on the polar vicinal SiC surfaces. Electron states caused by those atomic steps are also calculated, which assists in the identification of the atomic steps by future experiments.

DOI: [10.1103/PhysRevB.101.195307](https://doi.org/10.1103/PhysRevB.101.195307)

I. INTRODUCTION

Atomic steps are ubiquitous on surfaces of matters and exhibit various morphology, in particular, on semiconductor surfaces [1,2]. Such nanometer-scale structures occasionally accompanied by low dimensionality provide stages for new phenomena [3] such as flat-band magnetism on surfaces of nonmagnetic materials [4–6]. The surface steps also provide stages for materials syntheses: The epitaxial growth of thin films which is a central process of the fabrication of the electron devices occurs through the atomic reactions near the step edges [7,8]; even new materials emerge from surface steps, such as graphene from the silicon carbide (SiC) step through thermal decomposition [9–12]. The variation of the surface morphology involving the atomic steps has been discussed phenomenologically in terms of the surface kinetics [13,14]. Yet to unveil the underlying rationale behind the phenomena related to the atomic steps on the surface, the identification of abundant step structures and the clarification of the energetics of various atomic steps are indispensable and highly demanded in both science and technology. Up to now, however, only a few reports are available [15,16] which discuss the relation between the energetics of the atomic steps and the step morphology based on quantum theory.

In this paper, taking SiC as an example, we clarify the atomic and electronic structures and the energetics of the atomic steps on the basis of the first-principles calculations, and then reveal the atom-scale reason for the observed morphology variation.

SiC is a material studied for more than a century [17,18] and is widely used as hard ceramics. It is now emerging as a material for power electronics in semiconductor technology due to its superior properties such as the wide band gap, the

high electric break-down voltage, and the robustness under the harsh environment, compared to the current principal material, Si [8]. Actually, SiC metal-oxide-semiconductor field-effect transistors (MOSFETs) are already on the market. However, the performance of the current SiC-MOSFETs is still lower at present than what is expected from its intrinsic superior properties. The reason is presumably the lack of high-quality thin films.

Hexagonal SiC(0001) and cubic SiC(111) surfaces, which are the Si-face SiC polar surfaces, are commonly used for the SiC epitaxial growth. Many experiments revealed interesting characteristics in the step morphology on SiC(0001) and SiC(111) surfaces. The epitaxial growth is usually performed on the vicinal surface in which the low Miller-index surface is inclined by several degrees off toward a certain direction and there are variations of the step morphology depending on the inclined direction [19–22]. When the SiC(0001) surface is inclined toward the $(1\bar{1}00)$ direction, the step edge is straight. On the other hand, when the SiC(0001) surface is inclined toward the $(1\bar{1}\bar{2}0)$ direction, the step edge is meandering.

Despite the importance of the steps on SiC surfaces in science and technology, microscopic understanding from the theoretical side of the atomic and electronic structures of the steps is almost lacking: Only a few studies have been performed for the stepped SiC surfaces by using first-principles calculations so far, owing to the system size or its complexity of the modeling [6,16,23,24].

The aim of the present work is thus twofold. First, we perform total-energy electronic structure calculations that provide detailed atomic structures of all the possible atomic steps on SiC(0001) surfaces, the energetics of those steps, and the resulting electron states induced by the steps. The understanding obtained here is a firm theoretical framework

to consider the phenomena related to the atomic steps of SiC surfaces. Second, we reveal the reason for the morphology difference of atomic steps between $\langle 11\bar{2}0 \rangle$ and $\langle 1\bar{1}00 \rangle$ inclined (0001) vicinal surfaces. Our calculations clearly show that the energetics of the atomic steps is the reason for the observed morphology, indicating that the kinetic hindrances such as the diffusion barriers play minor roles in determining the morphology.

We recently reported the structure and the energetics of the distinct steps on SiC [25]. In this paper, we provide detailed explanations of the modeling and the calculations and present new results on the atomic and electronic structures. The rest of the present paper is organized as follows. Section II describes the theoretical methods applied and the modeling of atomic steps. In Sec. III, the results of the first-principles calculations including structural properties, energetics, and electronic properties are presented. In this section, we also present the reason for meandering step morphology during the SiC epitaxial growth and discuss the effect of the terrace reconstruction on the step edges. Section IV concludes the paper.

II. APPROACHES AND COMPUTATIONAL METHODS

A. Density-functional calculations

All calculations are performed on the basis of the density-functional theory (DFT) [26,27] within the generalized gradient approximation (GGA) introduced by Perdew, Burke, and Ernzerhof (PBE) [28]. We use the real-space DFT (RS-DFT) program code [29–31]. The RSDFT code is based on the real-space finite-difference pseudopotential method [32] and is powerful for parallel and large-scale calculations, as is evidenced by the Gordon Bell prize in 2011 [30]. Norm-conserving pseudopotentials are generated following the scheme of Troullier and Martins [33] to simulate nuclei and core electrons. In the real-space scheme, discrete grid points are introduced in real space, and the Hamiltonian in the Kohn-Sham (KS) equation in the DFT is expressed as a matrix represented at the grid points. The grid-point space of 0.20 Å, which is equivalent to a cutoff energy of ~ 68 Ry in the plane-wave-basis-set calculations, is found to suffice the present required accuracy. The geometry optimization is performed until the remaining forces on the atoms become less than 50 meV/Å. The Brillouin-zone integration is performed with enough sampling k points (see below).

B. Classification of step types

In this paper, we focus on single-bilayer height steps owing to the following reasons. In the pioneering work on the step-flow growth, the single-bilayer height steps are considered [34]. The step height of ~ 0.25 nm corresponding to the single-bilayer height is indeed observed [20,35,36]. Furthermore, the single-bilayer height step on the $4H$ -SiC(0001) surface has lower formation energy than the double- and quad-bilayer height steps from the previous DFT calculations [16].

SiC is an ambivalent semiconductor with its covalency and ionicity [37,38]: Electron is transferred from Si to C, whereas it takes the tetrahedrally bonded structure typical to covalent materials. This leads to a variety of polytypes in which atomic

stacking along the bond direction is different. They are named by the number of Si-C bilayers in the primitive cell and the symmetry, cubic (C), hexagonal (H), or rhombohedral (R), such as $2H$, $3C$, $4H$, $6H$, and $15R$ structures. We use $3C$ -SiC for polytypes in this work. This is reasonable since the difference among the polytypes is only in the atomic stacking and the local structure with the single-bilayer height step, which is important in considering the step morphology, is identical in all the polytypes. Nomenclature thus changes from $\{0001\}$ in the hexagonal symmetry to $\{111\}$ in the cubic symmetry, and also the $\langle 1\bar{1}00 \rangle$ and $\langle 11\bar{2}0 \rangle$ directions become the $\langle \bar{1}2\bar{1} \rangle$ and $\langle \bar{1}01 \rangle$ directions, respectively.

Stepped surfaces are modeled by a supercell structure that is periodic in all three directions. To simulate an isolated step on an otherwise flat surface, we use a periodic-array slab [39] and a vicinal slab [15,40] (see below) both of which have lateral superperiodicity. Each slab is periodically arranged along the surface normal direction with a thick-enough vacuum region. Regarding the structure of the surface terrace, we consider the (1×1) lateral periodicity and then optimize the structure including both the step and the terrace by relaxing the atoms in a supercell. Experimentally, the $(\sqrt{3} \times \sqrt{3})R30^\circ$ reconstruction is commonly observed [41–44]. Hence, we also examine the effect of such terrace reconstruction on the step structure. We consider the steps appearing on the (111) vicinal surface inclined toward either the $\langle \bar{1}2\bar{1} \rangle$ or $\langle \bar{1}01 \rangle$ direction. The step edge generally runs along the direction normal to $\langle \bar{1}2\bar{1} \rangle$ in the former case (we call it the $\langle \bar{1}2\bar{1} \rangle$ step hereafter), and in the latter case it does along the normal to $\langle \bar{1}01 \rangle$ (the $\langle \bar{1}01 \rangle$ step hereafter).

Figure 1(a) shows a schematic view of the five distinct steps on $3C$ -SiC(111) surfaces. For the $\langle \bar{1}01 \rangle$ step, there is a single type of the step edge at which both Si and C atoms appear. They are twofold and threefold coordinated, respectively, before the atomic relaxation. We call this step SC denoting Si and C. For the $\langle \bar{1}2\bar{1} \rangle$ step, there appear four distinct step types. We label them the atomic species at the step edge and the number of dangling bonds before the atomic relaxation: Si2, Si3, C1, and C2. Since the arrangements of the surface atoms are different toward the $[\bar{1}2\bar{1}]$ and $[\bar{1}2\bar{1}]$ directions, two particular types of the step edges appear for each direction. For the $[\bar{1}2\bar{1}]$ direction, the Si2 and C2 steps are possible, whereas for the $[\bar{1}2\bar{1}]$ direction the Si3 and C1 steps are possible [Fig. 1(b)].

C. Step formation energies

Now we introduce the formation energy λ_α of a particular step labeled α , for a periodic-array slab. Since the numbers of Si and C atoms near the step edge are different for different step types, one has to introduce the chemical potentials μ_i of each atomic species. Hence the step formation energy λ_α is given as

$$\sum_{\alpha} \lambda_{\alpha} L = E_{\text{step}} - E_{\text{flat}} - \sum_i \mu_i \Delta N_i, \quad (1)$$

where L is the length of the step edge in the lateral unit cell, E_{step} is the total energy obtained for the stepped periodic-array slab, E_{flat} is the total energy of the flat slab, ΔN_i is the difference in the number of atomic species i with respect to

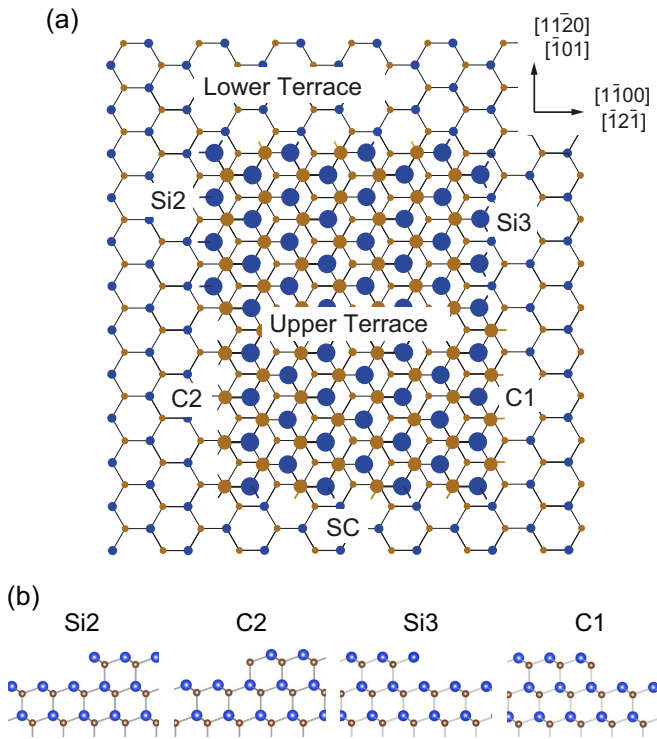


FIG. 1. (a) Schematic view of the five distinct single-bilayer height steps (Si2, Si3, C1, C2, and SC) on 3C-SiC(111) surfaces. The upper and lower terraces are depicted by the networks of the larger and smaller balls, respectively. (b) Side views of the step-edge structures for the four different $\langle 1\bar{2}1 \rangle$ steps before the atomic relaxation. Si and C atoms are represented by the blue and brown balls, respectively.

the flat slab. Geometry optimization of the flat slab results in the buckled configuration in which the top-layer Si atoms shift upwards and downwards alternately. This relaxation is similar to the obtained structure for 4H-SiC(0001) surfaces in the previous DFT calculation [45]. Hence, as the total energy of the flat slab in Eq. (1), we take that of the buckled (2×1) surface.

Since the system considered is in equilibrium with the SiC substrate, the chemical potentials of the individual species satisfy

$$\mu_{\text{Si}} + \mu_{\text{C}} = \varepsilon_{\text{SiC}}^{\text{bulk}}, \quad (2)$$

where $\varepsilon_{\text{SiC}}^{\text{bulk}}$ is the total energy of crystalline SiC per molecular unit. Then the formation energy (1) is expressed as a function of either μ_{Si} or μ_{C} . In this paper we take μ_{Si} as an independent variable. Then

$$\sum_{\alpha} \lambda_{\alpha} L = E_{\text{step}} - E_{\text{flat}} - \varepsilon_{\text{SiC}}^{\text{bulk}} \Delta N_{\text{C}} - \mu_{\text{Si}} (\Delta N_{\text{Si}} - \Delta N_{\text{C}}). \quad (3)$$

In a periodic-array slab, step edges appear at two sides of the terrace. For the $\langle 101 \rangle$ step, the two steps are SC identical to each other. However, as stated above, for the $\langle 1\bar{2}1 \rangle$ steps, either the C1 or Si3 step appears at one side and either C2 or Si2 does at the other side. Therefore, only four combinations are possible owing to the restriction of the symmetry of the

crystal, whereas the number of two combinations among four elements is intrinsically ${}^4C_2 = 6$. We obtain four equations for $\lambda_{\text{Si2}} + \lambda_{\text{C1}}$, $\lambda_{\text{C2}} + \lambda_{\text{Si3}}$, $\lambda_{\text{C2}} + \lambda_{\text{C1}}$ and $\lambda_{\text{Si2}} + \lambda_{\text{Si3}}$ as the left-hand side of Eq. (3). For the (Si2, C1) and (C2, Si3) step pairs, the step edges are terminated by both Si and C atoms. The differences in the number of Si and C atoms can be taken as $\Delta N_{\text{Si}} = \Delta N_{\text{C}}$ in this case. For the (C2, C1) step pair, the step edge is constructed by removing two Si atoms at the Si3 step in the (C2, Si3) step pair. Likewise, for the (Si2, Si3) step pair, the step edge is constructed by removing two C atoms from the C1 step in the (Si2, C1) step pair.

Only three of the four equations above for the sum of the formation energies are linear independent. We thus need additional equation among the formation energies. The simplest one is $\lambda_{\text{Si2}} - \lambda_{\text{C1}}$, $\lambda_{\text{C2}} - \lambda_{\text{Si3}}$, $\lambda_{\text{C2}} - \lambda_{\text{C1}}$, or $\lambda_{\text{Si2}} - \lambda_{\text{Si3}}$. These differences in the two formation energies are computed by using vicinal slabs since it is possible to contain a single step type: We prepare two vicinal slabs each of which contains a particular step type and compare the total energies of the slabs to get the formation-energy difference. Hence the difference between the formation energies of the steps α and β becomes

$$(\lambda_{\alpha} - \lambda_{\beta})L = E_{\text{step}(\alpha)} - E_{\text{step}(\beta)} - \sum_i \mu_i \Delta N_i, \quad (4)$$

where $E_{\text{step}(\alpha)}$ [$E_{\text{step}(\beta)}$] is the total energy of the vicinal slab which contains the step α (β), and ΔN_i is the number difference of atomic species i between the two vicinal slabs.

For the vicinal slabs the chemical potential of hydrogen μ_{H} should also be considered due to the difference of the total number of hydrogen atoms bonded to the bottom C atoms between the $[1\bar{2}1]$ and $[\bar{1}2\bar{1}]$ steps. The chemical potential of hydrogen μ_{H} is chosen as $\mu_{\text{H}} = (\varepsilon_{\text{CH}_4} - \mu_{\text{C}})/4$, where $\varepsilon_{\text{CH}_4}$ is the cohesive energy of a methane molecule. The step formation energy is thus expressed as a function of the Si chemical potential also in this case.

The heat of formation of SiC, ΔH_f , is defined by $\Delta H_f = \varepsilon_{\text{Si}}^{\text{bulk}} + \varepsilon_{\text{C}}^{\text{bulk}} - \varepsilon_{\text{SiC}}^{\text{bulk}}$, where $\varepsilon_{\text{Si}}^{\text{bulk}}$ and $\varepsilon_{\text{C}}^{\text{bulk}}$ are the total energies of the crystalline Si and diamond per atom, respectively. Although chemical potentials vary depending on experimental environments, there are the upper and lower limits. At those limits, the constituent element, Si or C, may precipitate. Hence the allowed range of the chemical potential for μ_{Si} is given by $\varepsilon_{\text{Si}}^{\text{bulk}} - \Delta H_f \leq \mu_{\text{Si}} \leq \varepsilon_{\text{Si}}^{\text{bulk}}$, representing the C-rich environment ($\mu_{\text{Si}} = \varepsilon_{\text{Si}}^{\text{bulk}} - \Delta H_f$) and the Si-rich environment ($\mu_{\text{Si}} = \varepsilon_{\text{Si}}^{\text{bulk}}$). We determined the theoretical value of ΔH_f by calculating the total energies of the crystalline Si, C, and 3C-SiC. For the diamond-structured Si, C, and 3C-SiC, we used the theoretical lattice constants of 5.48, 3.56, and 4.37 Å, respectively. The obtained heat of formation is 0.44 eV per SiC molecular unit for 3C-SiC, in agreement with other DFT results [46,47].

D. Slab models

Our periodic-array slab consists of 5 SiC bilayers and an additional SiC bilayer representing the upper terrace. The bottom side of the slab is passivated by hydrogen atoms. To simulate a $\langle 101 \rangle$ step, namely the SC step, we use a periodic-array slab with a $(16 \times \sqrt{3})$ lateral unit cell (see Fig. 2). For a $\langle 1\bar{2}1 \rangle$ step we use a $(2 \times 8\sqrt{3})$ lateral unit cell to preserve

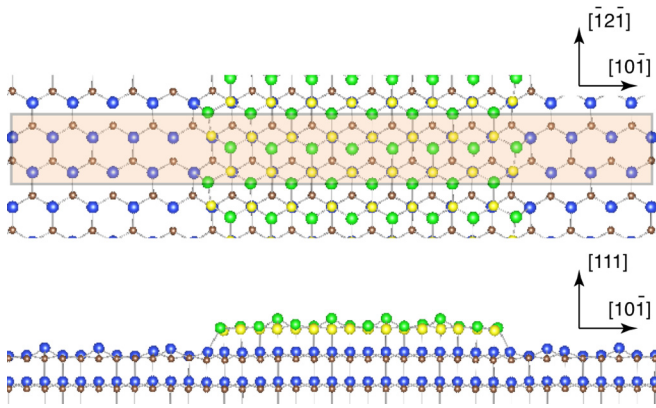


FIG. 2. Top and side views of the optimized structure of the SC steps using the periodic-array slab. Green: Si atoms on the terrace; yellow: C atoms on the terrace; blue: Si atoms; brown: C atoms. The highlighted region in the top view is the lateral surface unit cell.

the volume of the slabs for the two distinct steps to assure the numerical accuracy. Consequently, the terrace widths in the supercells for the $\langle 101 \rangle$ and $\langle 121 \rangle$ steps are 23.8 and 19.8 Å, respectively.

Our vicinal slab for a $\langle 121 \rangle$ step consists again of 5 SiC bilayers with the terrace and the step edge appearing periodically toward the $\langle 121 \rangle$ direction. In the unit cell, ten Si-C zigzag rows are included and the periodicity along the step edge is two times of the hexagonal lattice constant for each model. The terrace width for the vicinal slab depends on the inclined direction (see Fig. 3). At the bottom layer, C edge atoms appear with two or three dangling bonds which are passivated by H atoms. Hence either the CH₂ or CH₃ unit emerges at the bottom edge: Actually the CH₂ unit appears in the slab simulating the $[121]$ step (Si2 and C2 steps) and the CH₃ unit does in the slab for the $[121]$ step (Si3 and C1 steps).

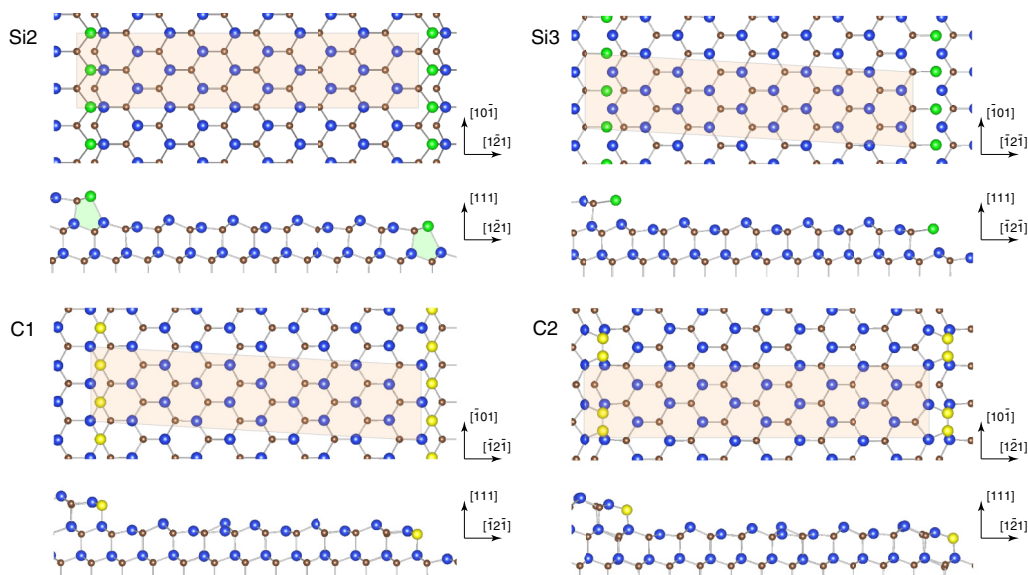


FIG. 3. Top and side views of optimized structures of the four $\langle 121 \rangle$ steps, Si2, Si3, C1, and C2, using the vicinal slabs. The color coding is Si atoms (blue), C atoms (brown), Si edge atoms (green), and C edge atoms (yellow). The lateral surface unit cells used are highlighted in the top views.

The lattice constant of SiC is fixed at the calculated value in the crystalline 3C-SiC of 4.37 Å, which is 3.092 Å as the hexagonal lattice constant a_{hex} , and agrees with the previous DFT-GGA result [48]. Each slab is isolated by $\gtrsim 10.5$ Å of the vacuum region from the adjacent images. The Brillouin-zone integration has been performed using the 4- k points along the step-edge direction.

III. RESULTS AND DISCUSSIONS

A. Structural properties and energetics

The optimized structure of the SC step obtained by using the periodic-array slab is shown in Fig. 2. A Si edge atom on the upper terrace rebonds with its neighboring Si atom on the lower terrace. This characteristic rebond was also found in the previous DFT calculations for the steps on 4H-SiC(0001) toward the $[11\bar{2}0]$ direction [16]. Similar rebond has been also discussed for steps on Si(001) surfaces [15,49] and on the Si(111) 2×1 surface [50]. The calculated rebond length, which is a key structural parameter of the SC step is 2.42–2.43 Å, in agreement with that of 2.43 Å in the previous DFT results [16]. This length is slightly longer than the bond length in the crystalline Si of 2.37 Å. However, it is much smaller than the Si-Si distance of 3.09 Å in the unrelaxed (ideal) single-bilayer height step. The neighboring C atoms of the Si edge atoms are highly strained. The Si-C bond lengths between the Si edge atom and its neighboring C atoms are 1.95 and 1.83 Å which are $\sim 5.3\%$ longer and $\sim 7.4\%$ shorter, respectively, than that in the crystalline SiC of 1.89 Å. The Si-C bond between the Si and C edge atoms has the shorter Si-C bond length. The bond angles surrounded by the upper-terrace Si and C edge atoms are 99° – 108° and 93° – 124° , respectively. The angles for the upper-terrace C edge atoms are close to the values for the C edge in the $(112n)$ ($n = 12$) nanofacet of 4H-SiC(0001) surfaces obtained by the previous DFT calculations [6].

Figure 3 shows the top and side views of stable structures of the four distinct $\langle\bar{1}2\bar{1}\rangle$ steps obtained by using the vicinal slabs. We also determined the step-edge structures for the $\langle\bar{1}2\bar{1}\rangle$ steps using the periodic-array slabs. The structural characteristics obtained by the different slab models are the same. Let us first focus on the relaxed geometries of the $\langle\bar{1}2\bar{1}\rangle$ steps with the Si edge atoms (Si2 and Si3 steps). At the Si2 step, an upper-terrace Si edge atom rebonds with its neighboring lower-terrace Si atom. Consequently, the rebonded upper-terrace Si edge atom is threefold coordinated. The rebond length ranges in 2.47–2.48 Å and is slightly longer than that in the SC step described above. The Si edge atoms form a five-membered ring marked by highlighted green areas in Fig. 3. The number of dangling bonds of the upper-terrace Si edge atom is reduced as a result of forming the rebonds.

At the Si3 step, the ideal distance between the upper- and lower-terrace Si edge atoms is equal to the hexagonal lattice constant $a_{\text{hex}} = 3.092$ Å. After the geometry optimization, the Si-Si distances among three Si atoms, one of the upper terrace and the two of the lower terrace, are 2.64–2.66 Å. These lengths are longer than the rebond lengths in the Si2 step and are elongated by about 12% compared to the bond length in the crystalline Si. This is indicative of the *weak covalent bond* between the upper- and lower-terrace Si atoms, which was discussed in defects in bulk materials [51,52]. As a consequence, the rebonded Si atoms on the lower terrace are fivefold coordinated with three covalent bonds and two weak covalent bonds, as occasionally observed in defective semiconductors [53], whereas the Si edge atoms on the upper terrace are threefold coordinated with one covalent bond and two weak covalent bonds. The number of dangling bonds of the upper-terrace Si edge atom is reduced from three to one.

Adding a single row of C atoms at the Si step edges leads to the C1 and C2 steps from the Si3 and Si2 steps, respectively. At the C1 step shown in Fig. 3, no striking geometrical change occurs at the step edge from the ideal atomic structure. We find that the bond lengths between the C edge atom and its nearest-neighbor Si atoms on the upper and lower terraces are 1.78 and 1.85 Å, respectively. These Si-C bond lengths are shorter than that in the crystalline SiC of 1.89 Å. The number of dangling bonds of the C edge atom still remains one.

Another structural characteristic is a dimerization which we found at the C2 step shown in Fig. 3. In the unrelaxed structure, one of the two dangling bonds at each C edge atom faces another dangling bond at the adjacent C edge atom. Hence, the dimerization along the step edges is expected. The dimerization indeed leads to the energy gain of 0.40 eV/Å. The dimer at the C2 step is found to be symmetric. The dimer bond length of 1.47 Å is longer than that of 1.38 Å for the symmetric dimer on the C(001) surfaces obtained by the previous DFT-GGA calculations [54], but shorter than the bond length in the crystalline diamond of 1.54 Å. We find the dimerization at the C2 steps also in the periodic-array slabs with the dimer bond length of 1.47 Å, being identical to that in the vicinal slab. The number of dangling bonds of the C edge atom decreases as a consequence of the dimerization.

The bonds of the edge atoms are highly strained with the bond stretching for the Si2, Si3, and C2 steps. In particular, a significant distortion arises from the C-C dimers for the C2 step and causes the strain energy. All step-edge types have one

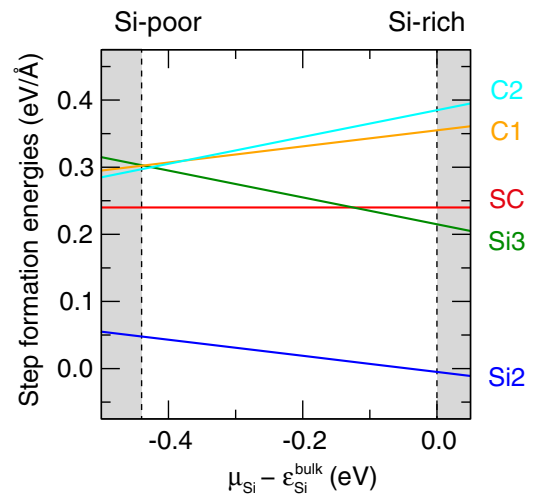


FIG. 4. Calculated formation energies of the atomic steps, SC (red line), Si2 (blue line), Si3 (green line), C1 (orange line), and C2 (light blue line), on 3C-SiC(111) surfaces as a function of the Si chemical potential μ_{Si} . The vertical dashed lines denote the range of $\mu_{\text{Si}} - \epsilon_{\text{Si}}^{\text{bulk}}$. The Si-rich (C-poor) and Si-poor (C-rich) limits correspond to the right and left sides, respectively.

remaining unsaturated dangling bond at the edge atoms after the atomic relaxation. The remaining dangling bonds at the edge atoms are expected to be reactive in the epitaxial growth, etching process, and so forth.

Figure 4 shows the calculated formation energies of the five distinct steps as a function of the Si chemical potential $\mu_{\text{Si}} - \epsilon_{\text{Si}}^{\text{bulk}}$. We find that the Si2 step is energetically most favorable. The Si3 step is the next in the Si-rich condition. In the C-rich condition, the SC step is the second lowest in the formation energy. The C edge steps are energetically unfavorable. We find that the C1 and C2 steps have almost equal formation energies for the allowed range of μ_{Si} . There is uncertainty in the calculated formation energies for the steps on the $\langle\bar{1}2\bar{1}\rangle$ vicinal surface. As stated in Sec. II C, we used four distinct slabs to determine the formation energies of Si2, Si3, C1, and C2 individually, and then the choice of the four slabs are arbitrary. We examined various choices and found that the uncertainty was less than 35 meV/Å, representing the cutting-edge accuracy of the present calculations.

In Fig. 4, we unequivocally clarified that the Si2 step and also the Si3 step in the Si-rich condition, which belong to the $\langle\bar{1}2\bar{1}\rangle$ step, were energetically more favorable than the $\langle\bar{1}0\bar{1}\rangle$ step, i.e., the SC step. This finding was important to discuss the step morphology experimentally observed. The scanning tunneling microscopy (STM) observations by Chang *et al.* [55] showed that the step edges are aligned in the $\langle\bar{1}0\bar{1}\rangle$ directions on the 3C-SiC (111) surfaces, corresponding to the straight $\langle\bar{1}2\bar{1}\rangle$ step. Also for hexagonal SiC(0001) surfaces inclined toward the $\langle 1\bar{1}00 \rangle$ direction, straight stripe-type morphology was observed [19–22,56]. Our results above naturally explain these experimental findings in the past. Furthermore, the spiral patterns were reported for on-axis hexagonal SiC(0001) surfaces [56–58]. Isolated hexagonal hillocks are formed and every step is perpendicular to one of the six equivalent $\langle 1\bar{1}00 \rangle$ directions, which corresponds

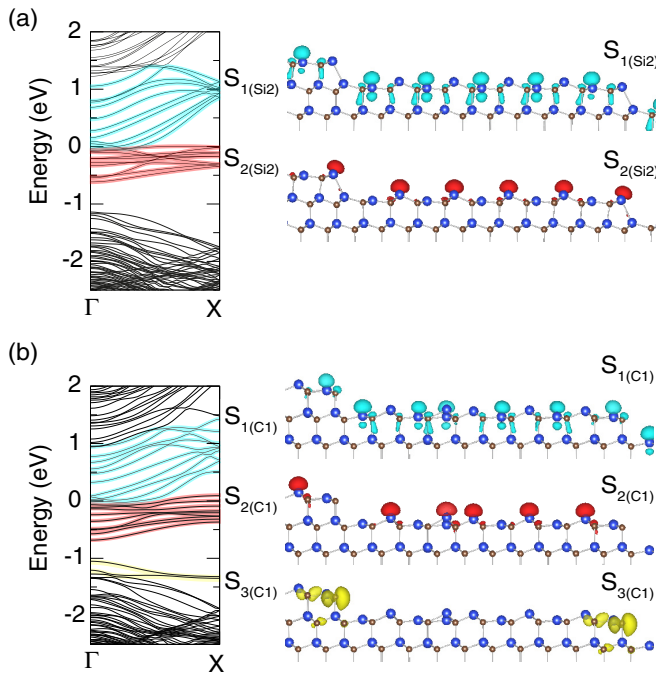


FIG. 5. Electronic band structures along the step edge (ΓX direction) and the Kohn-Sham orbitals at the Γ point for (a) the Si2 step and (b) the C1 step. The Fermi levels are set to be zero. The isovalue surfaces at 25 % of their maximum values are shown. Blue and brown balls depict Si and C atoms, respectively.

to the $\langle \bar{1}2\bar{1} \rangle$ direction in the cubic case. Our calculated step formation energies also provide a natural explanation for those spiral patterns.

B. Electronic structures

The characteristic atomic structures of the five steps, SC, Si2, Si3, C1, and C2, are presented in Sec. III A. Their electron densities and density of states were already shown in our recent papers in Refs. [25] and [59], respectively. We here perform the electronic structure calculations for the two steps among the five distinct steps using vicinal slabs: One is the Si2 step which has the lowest step formation energy and the other is the C1 step which is an example different from the Si2 step in both the edge-atom species and the inclined direction. The calculated band structures along the ΓX direction parallel to the step edge for the Si2 and C1 steps together with their KS orbitals are shown in Fig. 5. The valence band maximum of bulk 3C-SiC is set to be zero at the ordinate. The two band structures have similar features except for the flat bands near the top of the valence bands for the C1 step. The calculated energy gap of bulk 3C-SiC is 1.41 eV, which agrees well with the other first-principles calculations within DFT-GGA [48], and underestimated by 40% typical to the local and semilocal approximations for the exchange-correlation energy functional.

For the (2×1) buckled step-free surfaces, the dangling bond states appear in the bulk band gap [60]. We indeed observe the states originating from the dangling bonds of the terrace Si atoms in the bulk band gap in the region between 0 and 1.4 eV for the Si2 and C1 steps. Those gap states

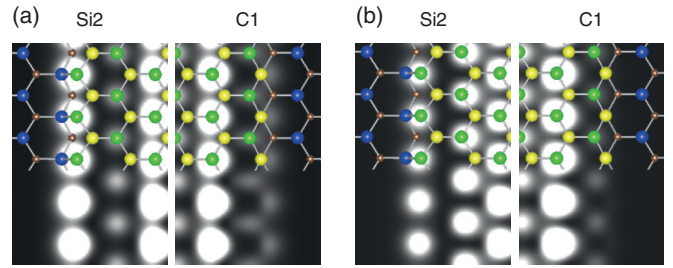


FIG. 6. Calculated STM images in the vicinity of the Si2 and C1 steps for (a) -1.5 V and (b) $+1.0$ V bias voltages using the periodic-array slab. The color coding of balls is the same as in Fig. 2. The upper terrace is located at the right (left) side for the Si2 (C1) step.

are partially occupied. In Fig. 5, at the Si2 step, the group of the energy bands labeled $S_{2(\text{Si}2)}$ is occupied, whereas the group labeled $S_{1(\text{Si}2)}$ is unoccupied. Likewise, the groups of the energy bands labeled $S_{1(\text{C}1)}$ and $S_{2(\text{C}1)}$ are unoccupied and occupied, respectively, for the C1 step.

The groups of the occupied surface states, $S_{2(\text{Si}2)}$ and $S_{2(\text{C}1)}$, show a similar character. They are distributed at the dangling bonds of the terrace Si atoms which shift upwards. The groups of the unoccupied surface states, $S_{1(\text{Si}2)}$ and $S_{1(\text{C}1)}$, at the Si2 and C1 steps have characters in common. The main contribution to the $S_{1(\text{Si}2)}$ and $S_{1(\text{C}1)}$ groups originates from the empty dangling bonds of the terrace Si atoms shifting downwards. A dominant contribution to the $S_{3(\text{C}1)}$ group apparently comes from the C edge atoms, whereas the contribution from the Si edge atoms appears in the $S_{2(\text{Si}2)}$ group.

Those characteristics on the energy-band structures are observable by, e.g., STM. Figure 6 shows the calculated STM images of the Si2 and C1 steps using the periodic-array slab. The STM images are simulated according to the scheme of Tersoff and Hamann [61]. The difference between the two steps is clear in the occupied-state images. We observe bright spots corresponding to the rebonding of the upper- and lower-terrace Si edge atoms in the vicinity of the Si2 step edge, whereas at the C1 step the spots are relatively dark due to the lack of the edge-carbon character in the relevant electron states [$S_{2(\text{C}1)}$ in Fig. 5(b)] contributing the occupied-state STM image. In the unoccupied-state STM images the bright spots corresponding to the dangling bonds on the Si atoms are primarily observed.

C. Zigzag-shaped step structures

The meandering step morphology toward the $\langle 11\bar{2}0 \rangle$ direction on hexagonal SiC(0001) surfaces are observed by experiments [19–22,62]. A possibility to explain this meandering is the energetics. In Sec. III A, we clearly showed that some of the $\langle \bar{1}2\bar{1} \rangle$ steps have lower formation energies than that of the $\langle \bar{1}01 \rangle$ step on 3C-SiC(111) surfaces. It is therefore plausible that a zigzag-shaped step toward the $\langle \bar{1}01 \rangle$ direction, which consists of the local straight $\langle \bar{1}2\bar{1} \rangle$ steps, is energetically more favorable than the straight SC step toward the $\langle \bar{1}01 \rangle$ direction shown in Figs. 1(a) and 2.

A step model with a zigzag configuration along the $\langle 11\bar{2}0 \rangle$ direction on 6H-SiC(0001) as a hexagonal counterpart was proposed based on the STM observation [20]. The model

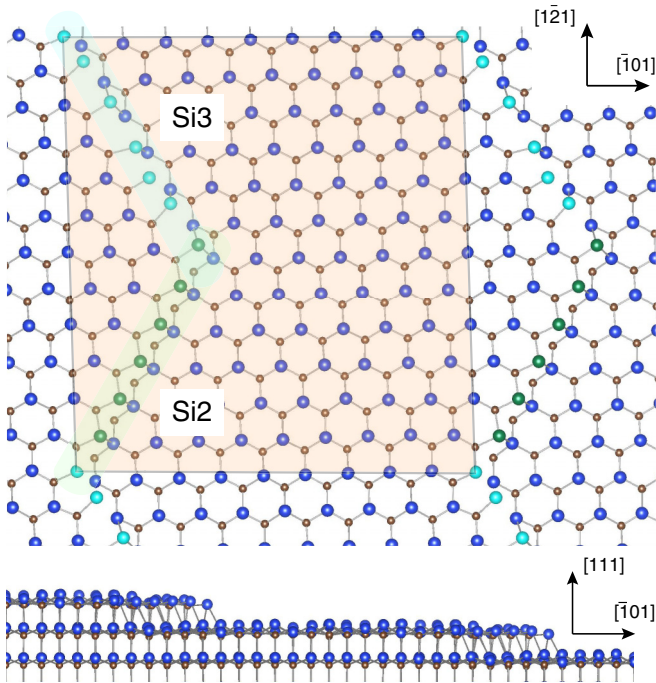


FIG. 7. Top and side views of the optimized atomic structure of the zigzag-shaped step consisting of the two local Si2 and Si3 steps shown in Fig. 3. The lateral surface unit cell is indicated by the highlighted orange region. The local Si2 and Si3 steps are marked with the green and light blue regions. The color coding is Si atoms (blue), C atoms (brown), Si edge atoms at Si2 (green), and Si edge atoms at Si3 (light blue).

has two step edges extended either along the $[\bar{2}110]$ and $[\bar{1}210]$ direction. The two step edges in this proposed model correspond to the Si2 and C1 steps in our terminology. Other zigzag-shaped steps consisting of the two local straight $\langle\bar{1}2\bar{1}\rangle$ steps are possible: the combinations of (C1, C2), (Si2, Si3), and (C2, Si3). From the formation energies of the straight steps shown in Fig. 4, it is clear that the combination (Si2, Si3) is the candidate which has the lowest formation energy of all of them. Therefore, we consider the zigzag-shaped step consisting of the two local Si2 and Si3 steps (“Si2+Si3 zigzag-shaped step” hereafter) and compare the stability between this zigzag-shaped step and the straight SC step.

A larger unit cell is necessary to describe the zigzag-shaped step. The large-scale calculations were performed for the unit cell containing the local Si2 and Si3 steps with their edge lengths being six times of the hexagonal lattice constant (Fig. 7). To save the computational cost, we reduce one SiC bilayer for the slab thickness, which still ensures the required accuracy as we tested. Nevertheless, 1050 atoms are required to simulate the Si2+Si3 zigzag-shaped step on the vicinal 3C-SiC(111) surfaces inclined toward the $[\bar{1}01]$ direction. The Γ -point Brillouin-zone sampling has been used.

We now present the formation-energy difference between the Si2+Si3 zigzag-shaped step and the straight SC step toward the $[\bar{1}01]$ direction. We found that the formation energy of the Si2+Si3 zigzag-shaped step is lower than that of the straight SC step by 4.30 and 1.66 eV per unit cell in the Si-rich and Si-poor conditions, respectively. By dividing these values

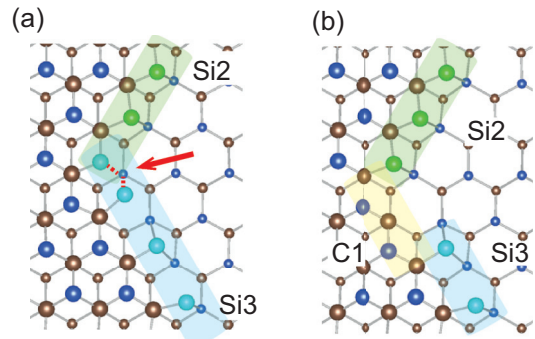


FIG. 8. Top views of the two possible local atomic structures near the kink of the zigzag-shaped step model shown in Fig. 7. The color coding is the same as in Fig. 7.

by the length of the straight step edge, we obtain the formation energy of the zigzag-shaped step being lower than that of the straight SC step by 0.05–0.13 eV/Å for μ_{Si} in the range of $\epsilon_{\text{Si}}^{\text{bulk}} - \Delta H_f \leq \mu_{\text{Si}} \leq \epsilon_{\text{Si}}^{\text{bulk}}$. The Si2+Si3 zigzag-shaped step is thus energetically more favorable than the straight SC step, being indicative of the stability of the meandering for the steps toward the $[\bar{1}01]$ direction. The energetics obtained here naturally explains the observed meandering step inclined toward the $\langle 11\bar{2}0 \rangle$ direction in the hexagonal case [19–22,62].

In Fig. 7, the atomic structure at the local Si2 and Si3 steps is essentially the same as the structures shown in Fig. 3. At the local Si2 step, the rebonding arises from the upper- and lower-terrace Si edge atoms and this is a similar feature to the Si2 step as described in Sec. III A. The rebond lengths range 2.45–2.51 Å and the average value is 2.48 Å. This is close to the value of 2.47 Å in the straight Si2 step toward the $\langle\bar{1}2\bar{1}\rangle$ direction. We find that the shortest rebond at the local Si2 step is located near the kink of the zigzag-shaped step.

At the local Si3 step, we find not only a weak covalent bond as mentioned in Sec. III A but also a rebond between upper- and lower-terrace Si edge atoms. Many of the lower-terrace Si atoms at the step edge change their coordination number from 5 to 4 probably due to the increased degrees of freedom for the reconstruction along the straight part.

At the kink where the Si2 and Si3 steps meet, we find two distinct (meta)stable geometries shown in Fig. 8. In Fig. 8(a), one lower-terrace Si atom (marked by the red arrow) and two upper-terrace Si edge atoms are rebonded (the red dashed lines). As a consequence, the lower-terrace Si atom becomes fivefold coordinated, being similar to the Si3 step toward the $\langle\bar{1}2\bar{1}\rangle$ direction. When one of the upper-terrace Si edge atoms near the kink at the Si3 step in Fig. 8(a) is removed, the upper-terrace C edge atom at the kink becomes threefold coordinated, being the local C1 step shown in Fig. 8(b). We find that the energies to form those kinks are almost the same.

D. Effect of the terrace reconstruction on the step edge

The Si-face cubic SiC(111) and hexagonal SiC(0001) surfaces have various surface reconstruction. As an example of a terrace reconstruction, we focus on the $(\sqrt{3} \times \sqrt{3})R30^\circ$ reconstruction in this work. It is known that the model with Si adatom on the T4 site which is the on-top site of an underlying

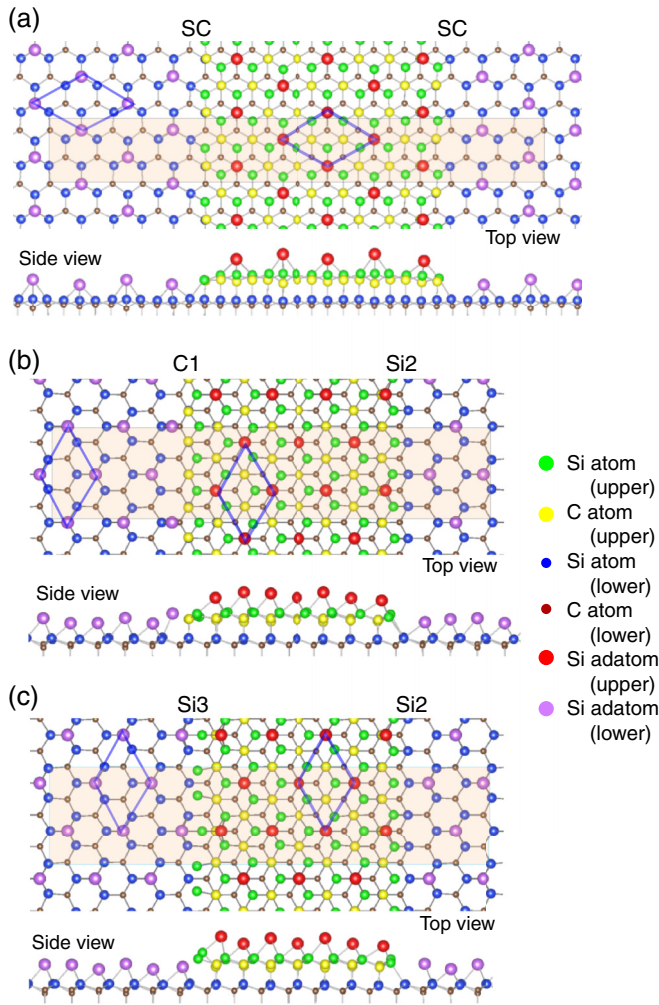


FIG. 9. Top and side views of the optimized structures of stepped 3C-SiC(111) surfaces with Si adatoms using periodic-array slabs (a) for the two SC steps, (b) for the (Si2, C1) step pair, and (c) for the (Si2, Si3) step pair. The separate color coding for the atoms on the upper terrace (upper) and the lower terrace (lower) is used. The $\sqrt{3} \times \sqrt{3}$ units are shown by the blue solid lines. The lateral surface unit cells used are highlighted in the top views.

second layer atom is most favorable for the $(\sqrt{3} \times \sqrt{3})R30^\circ$ reconstruction [43,44,46,63,64]. We use the periodic-array slabs to model the $\sqrt{3} \times \sqrt{3}$ -reconstructed terrace. We consider three models shown in Fig. 9: one model for the $\langle \bar{1}01 \rangle$ steps and two models for the $\langle \bar{1}2\bar{1} \rangle$ steps. The model of the $\langle \bar{1}01 \rangle$ step has two SC steps on the terrace. We use the models with the (Si2, Si3) and (Si2, C1) step pairs for the $\langle \bar{1}2\bar{1} \rangle$ steps since the Si2 step is most stable for the $\langle \bar{1}2\bar{1} \rangle$ direction. There are several distinct structural arrangements for each pair of steps, depending on the distances between the step edge and the Si adatoms on the terrace. We find that the geometries in which the Si adatoms are located at the edge sites are generally higher in energy.

Figure 9 shows the step-edge structures which has the minimum formation energies. We observe the rebonding between the upper- and lower-terrace Si edge atoms for the local SC and Si2 steps. This is essentially identical to the

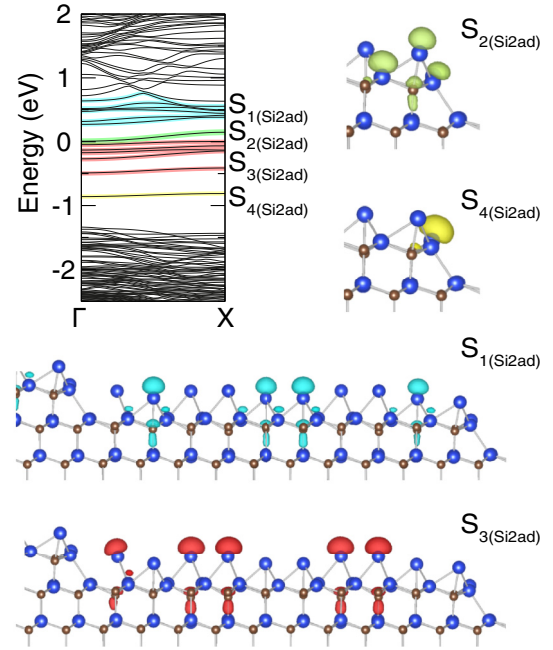


FIG. 10. Electronic band structure along the ΓX direction and the Kohn-Sham orbitals at the Γ point for the Si2 step on the $\sqrt{3} \times \sqrt{3}$ -reconstructed terrace. The isovalue surfaces at their value of 25% of the maximum value. Blue and brown balls depict Si and C atoms, respectively.

case of the (1×1) reconstruction shown in Figs. 2 and 3. The rebond lengths are 2.47–2.52 Å and 2.55–2.59 Å for the SC and Si2 steps, respectively, in this case. A weak covalent bond between the upper- and lower-terrace Si edge atoms is also found at the Si3 step with the $\sqrt{3} \times \sqrt{3}$ -reconstructed terrace. We find that the order of the formation energies, $2\lambda_{\text{SC}} > \lambda_{\text{Si2}} + \lambda_{\text{C1}} > \lambda_{\text{Si2}} + \lambda_{\text{Si3}}$, in the Si-rich limit and, $2\lambda_{\text{SC}} > \lambda_{\text{Si2}} + \lambda_{\text{Si3}} > \lambda_{\text{Si2}} + \lambda_{\text{C1}}$, in the C-rich limit remains unchanged, compared to the case of the (1×1) terrace structure. Taking the $(\sqrt{3} \times \sqrt{3})R30^\circ$ reconstruction as an example, we clarified that the terrace reconstruction plays only a minor role in the atomic structures at the step edges and their energetics [59].

Figure 10 shows the electronic band structure of the Si2 step with the $\sqrt{3} \times \sqrt{3}$ -reconstructed terrace. In this calculation, we use a vicinal slab. In the band structure we find the flat bands or the groups of the flat bands labeled $S_1(\text{Si2ad})$, $S_2(\text{Si2ad})$, $S_3(\text{Si2ad})$, and $S_4(\text{Si2ad})$ in the bulk band gap. The $S_1(\text{Si2ad})$ group and the $S_2(\text{Si2ad})$ band are unoccupied bands, whereas the $S_3(\text{Si2ad})$ group and the $S_4(\text{Si2ad})$ band are occupied ones. The contribution of the step edge atoms is found in the $S_2(\text{Si2ad})$ and $S_4(\text{Si2ad})$ states shown in Fig. 10. The KS orbitals for the $S_1(\text{Si2ad})$ and $S_3(\text{Si2ad})$ groups in Fig. 10 clearly show that those groups of the energy bands originate from the dangling bonds of the Si adatoms. However, the Si adatoms contributing to the $S_1(\text{Si2ad})$ and $S_3(\text{Si2ad})$ states are clearly different: the lower Si adatom to $S_1(\text{Si2ad})$ and the higher Si adatom to $S_3(\text{Si2ad})$. The bond lengths between the Si adatom and the top-layer Si atom are 1.52–1.56 Å and 1.93–1.95 Å for the Si adatoms contributing to the $S_1(\text{Si2ad})$ and $S_3(\text{Si2ad})$ groups, respectively. Their average value of 1.72 Å is in good

agreement with the experimental and theoretical values of 1.61–1.77 Å [43,44,46,63,64]. The different height of the Si-adatom positions comes from the buckling of the Si adatoms on the terrace.

IV. CONCLUSION

We carried out density-functional calculations of single-bilayer height steps on 3C-SiC(111) surfaces. Five types of steps appearing on the (111) vicinal surface inclined toward either the $\langle\bar{1}2\bar{1}\rangle$ or $\langle\bar{1}01\rangle$ direction were considered. We performed geometry optimization for all the possible atomic steps and found the characteristic atomic structures near the step edges. The calculated formation energies of the five distinct steps show that the straight $\langle\bar{1}2\bar{1}\rangle$ step is energetically more favorable than the straight $\langle\bar{1}01\rangle$ step. The most stable straight step has a rebonded structure with threefold-coordinated Si edge atoms on the upper terrace. We compared the formation energies between the straight $\langle\bar{1}01\rangle$ step and the zigzag-shaped $\langle\bar{1}01\rangle$ step consisting of the two local straight $\langle\bar{1}2\bar{1}\rangle$ steps and found that the latter is energetically favorable. The obtained energetics clearly explains experimental findings of the stability not only of the straight step toward the $\langle\bar{1}100\rangle$ direction in the hexagonal case ($\langle\bar{1}2\bar{1}\rangle$ direction in the cubic case), but also of the meandering step toward the $\langle\bar{1}1\bar{2}0\rangle$ direction in the hexagonal case ($\langle\bar{1}01\rangle$ direction in the cubic case). The structural feature and the energetics of steps on 3C-SiC(111) surfaces are essentially the same for (1×1) and $(\sqrt{3}\times\sqrt{3})R30^\circ$ reconstructions on the terrace.

The results of electronic band structures show that specific groups of the energy bands in the bulk band gap originate from the dangling bonds of the terrace Si atoms and the step-edge atoms. The calculated scanning tunneling microscopy images assist in further identification of the atomic structures of the surface steps.

We showed the causality between the energetics of the steps and the surface morphology of Si-face SiC polar surfaces, i.e., 3C-SiC(111) and equivalently hexagonal SiC(0001). Our calculations offer a missing link between microscopic atomic structures and macroscopic surface morphology. The obtained results from the present calculations certainly expand our understanding of the stages at which chemical reactions of the thin-film growth take place.

ACKNOWLEDGMENTS

The authors acknowledge financial support from the Ministry of Education, Culture, Sports, Science, and Technology (MEXT), Japan, under the program “Priority issue on post-K computer” (creation of new functional devices and high-performance materials to support next-generation industries; CDMSI) and also under the Contract No. 18H03873 of the grants-in-aid. We gratefully acknowledge a grant of super-computer time provided by the K Computer at the Advanced Institute for Computational Science, RIKEN, at the Super-computer Center, ISSP, The University of Tokyo, and at the Research Center for Computational Science at the National Institutes of Natural Sciences.

-
- [1] V. A. Shchukin and D. Bimberg, *Rev. Mod. Phys.* **71**, 1125 (1999).
- [2] J. Stangl, V. Holý, and G. Bauer, *Rev. Mod. Phys.* **76**, 725 (2004).
- [3] C. Tegenkamp, *J. Phys.: Condens. Matter* **21**, 013002 (2008).
- [4] S. Okada, K. Shiraishi, and A. Oshiyama, *Phys. Rev. Lett.* **90**, 026803 (2003).
- [5] S. C. Erwin and F. J. Himpsel, *Nat. Commun.* **1**, 58 (2010).
- [6] K. Sawada, J.-I. Iwata, and A. Oshiyama, *Phys. Rev. B* **93**, 235421 (2016).
- [7] See, e.g., *Advances in the Understanding of Crystal Growth Mechanisms*, edited by T. Nishinaga, K. Nishioka, J. Harada, A. Sasaki, and H. Takei, (Elsevier, New York, 1997).
- [8] T. Kimoto and J. A. Cooper, *Fundamentals of Silicon Carbide Technology* (John Wiley & Sons, Singapore, 2014).
- [9] J. Hass, W. A. de Heer, and E. H. Conrad, *J. Phys.: Condens. Matter* **20**, 323202 (2008).
- [10] K. V. Emtsev, A. Bostwick, K. Horn, J. Jobst, G. L. Kellogg, L. Ley, J. L. McChesney, T. Ohta, S. A. Reshanov, J. Röhr, E. Rotenberg, A. K. Schmid, D. Waldmann, H. B. Weber, and T. Seyller, *Nat. Mater.* **8**, 203 (2009).
- [11] S. Tanaka, K. Morita, and H. Hibino, *Phys. Rev. B* **81**, 041406(R) (2010).
- [12] N. Mishra, J. Boeckl, N. Motta, and F. Iacopi, *Phys. Status Solidi A* **213**, 2277 (2016).
- [13] E. D. Williams, *Surf. Sci.* **299–300**, 502 (1994).
- [14] C. Misbah, O. Pierre-Louis, and Y. Saito, *Rev. Mod. Phys.* **82**, 981 (2010).
- [15] A. Oshiyama, *Phys. Rev. Lett.* **74**, 130 (1995).
- [16] K. Sawada, J.-I. Iwata, and A. Oshiyama, *Appl. Phys. Lett.* **104**, 051605 (2014).
- [17] H. Baumhauer, *Z. Kristallogr.* **50**, 33 (1912).
- [18] C. L. Burdick and E. A. Owen, *J. Am. Chem. Soc.* **40**, 1749 (1918).
- [19] T. Ueda, H. Nishino, and H. Matsunami, *J. Cryst. Growth* **104**, 695 (1990).
- [20] S. Tanaka, R. Kern, R. F. Davis, J. F. Wendelken, and J. Xu, *Surf. Sci.* **350**, 247 (1996).
- [21] S.-I. Nakamura, T. Kimoto, H. Matsunami, S. Tanaka, N. Teraguchi, and A. Suzuki, *Appl. Phys. Lett.* **76**, 3412 (2000).
- [22] S. Nie, C. D. Lee, R. M. Feenstra, Y. Ke, R. P. Devaty, W. J. Choyke, C. K. Inoki, T. S. Kuan, and G. Gu, *Surf. Sci.* **602**, 2936 (2008).
- [23] C. Raffy, L. Magaud, E. Blanquet, M. Pons, and A. Pasturel, *Mater. Sci. Forum* **353–356**, 111 (2001).
- [24] E. Wachowicz, T. Ossowski, and A. Kiejna, *Appl. Surf. Sci.* **420**, 129 (2017).
- [25] K. Seino and A. Oshiyama, *Appl. Phys. Express* **13**, 015506 (2020).
- [26] P. Hohenberg and W. Kohn, *Phys. Rev.* **136**, B864 (1964).
- [27] W. Kohn and L. J. Sham, *Phys. Rev.* **140**, A1133 (1965).
- [28] J. P. Perdew, K. Burke, and M. Ernzerhof, *Phys. Rev. Lett.* **77**, 3865 (1996).

- [29] J.-I. Iwata, D. Takahashi, A. Oshiyama, T. Boku, K. Shiraishi, S. Okada, and K. Yabana, *J. Comput. Phys.* **229**, 2339 (2010).
- [30] Y. Hasegawa, J.-I. Iwata, M. Tsuji, D. Takahashi, A. Oshiyama, K. Minami, T. Boku, H. Inoue, Y. Kitazawa, I. Miyoshi, and M. Yokokawa, *Int. J. High Perform. Comput. Appl.* **28**, 335 (2014).
- [31] J.-I. Iwata, <https://github.com/j-iwata/RSDFT>.
- [32] J. R. Chelikowsky, N. Troullier, K. Wu, and Y. Saad, *Phys. Rev. B* **50**, 11355 (1994).
- [33] N. Troullier and J. L. Martins, *Phys. Rev. B* **43**, 1993 (1991).
- [34] H. Matsunami and T. Kimoto, *Mater. Sci. Eng., R* **20**, 125 (1997).
- [35] T. Kimoto, Z. Y. Chen, S. Tamura, S.-I. Nakamura, Nakamura, N. Onojima, and H. Matsunami, *Jpn. J. Appl. Phys.* **40**, 3315 (2001).
- [36] G. R. Yazdi, R. Vasiliauskas, T. Iakimov, A. Zakharov, M. Syväjärvi, and R. Yakimova, *Carbon* **57**, 477 (2013).
- [37] A. Qteish, V. Heine, and R. J. Needs, *Phys. Rev. B* **45**, 6534 (1992).
- [38] M. Sabisch, P. Krüger, and J. Pollmann, *Phys. Rev. B* **51**, 13367 (1995).
- [39] B. D. Yu and M. Scheffler, *Phys. Rev. B* **55**, 13916 (1997).
- [40] X.-P. Li, D. Vanderbilt, and R. D. King-Smith, *Phys. Rev. B* **50**, 4637 (1994).
- [41] A. van Bommel, J. Crombeen, and A. van Tooren, *Surf. Sci.* **48**, 463 (1975).
- [42] P. Mårtensson, F. Owman, and L. I. Johansson, *Phys. Status Solidi B* **202**, 501 (1997).
- [43] U. Starke, J. Schardt, J. Bernhardt, M. Franke, and K. Heinz, *Phys. Rev. Lett.* **82**, 2107 (1999).
- [44] A. Coati, M. Sauvage-Simkin, Y. Garreau, R. Pinchaux, T. Argunova, and K. Aïd, *Phys. Rev. B* **59**, 12224 (1999).
- [45] J. Olander and K. Larsson, *J. Phys. Chem. B* **105**, 7619 (2001).
- [46] M. Sabisch, P. Krüger, and J. Pollmann, *Phys. Rev. B* **55**, 10561 (1997).
- [47] P. Käckell, J. Furthmüller, and F. Bechstedt, *Diam. Relat. Mater.* **6**, 1346 (1997).
- [48] Y.-I. Matsushita and A. Oshiyama, *J. Phys. Soc. Jpn.* **86**, 054702 (2017).
- [49] D. J. Chadi, *Phys. Rev. Lett.* **59**, 1691 (1987).
- [50] R. M. Feenstra and J. A. Stroscio, *Phys. Rev. Lett.* **59**, 2173 (1987).
- [51] M. Saito and A. Oshiyama, *Phys. Rev. Lett.* **73**, 866 (1994).
- [52] J.-I. Iwata, K. Shiraishi, and A. Oshiyama, *Phys. Rev. B* **77**, 115208 (2008).
- [53] S. T. Pantelides, *Phys. Rev. Lett.* **57**, 2979 (1986).
- [54] J. A. Steckel, G. Kresse, and J. Hafner, *Phys. Rev. B* **66**, 155406 (2002).
- [55] C. Chang, I. Tsong, Y. Wang, and R. Davis, *Surf. Sci.* **256**, 354 (1991).
- [56] W. Wulfhekkel, D. Sander, S. Nitsche, F. Dulot, A. Leycuras, and M. Hanbücken, *Surf. Sci.* **550**, 8 (2004).
- [57] J. A. Powell and D. J. Larkin, *Phys. Status Solidi B* **202**, 529 (1997).
- [58] S.-I. Nakamura, T. Kimoto, and H. Matsunami, *Jpn. J. Appl. Phys.* **42**, L846 (2003).
- [59] K. Seino and A. Oshiyama, *Mater. Sci. Forum* (to be published).
- [60] T. Kaneko, T. Yamasaki, N. Tajima, and T. Ohno, *Surf. Sci.* **647**, 45 (2016).
- [61] J. Tersoff and D. R. Hamann, *Phys. Rev. B* **31**, 805 (1985).
- [62] K. Hayashi, K. Morita, S. Mizuno, H. Tochiyama, and S. Tanaka, *Surf. Sci.* **603**, 566 (2009).
- [63] J. E. Northrup and J. Neugebauer, *Phys. Rev. B* **52**, R17001 (1995).
- [64] M. C. Righi, C. A. Pignedoli, G. Borghi, R. Di Felice, C. M. Bertoni, and A. Catellani, *Phys. Rev. B* **66**, 045320 (2002).